

San Jose State University

From the Selected Works of Minghui Diao

June 12, 2014

Hemispheric Comparison of Cirrus Cloud Evolution Using in Situ Measurements in HIAPER Pole-to-Pole Observations

Minghui Diao, *National Center for Atmospheric Research*

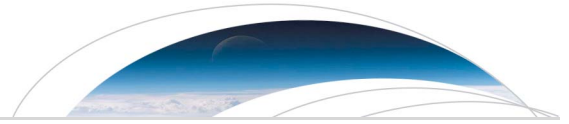
Mark A. Zondlo, *Princeton University*

Andrew J. Heymsfield, *National Center for Atmospheric Research*

Stuart P. Beaton, *National Center for Atmospheric Research*



Available at: <https://works.bepress.com/minghui-diao/2/>



RESEARCH LETTER

10.1002/2014GL059873

Key Points:

- Ice supersaturation frequencies comparable between hemispheres
- Microphysics of cirrus clouds follow similar evolution between hemispheres
- Relative timescale for each cirrus evolution phase is similar between NH and SH

Correspondence to:

M. A. Zondlo,
mzondlo@princeton.edu

Citation:

Diao, M., M. A. Zondlo, A. J. Heymsfield, and S. P. Beaton (2014), Hemispheric comparison of cirrus cloud evolution using in situ measurements in HIAPER Pole-to-Pole Observations, *Geophys. Res. Lett.*, 41, 4090–4099, doi:10.1002/2014GL059873.

Received 10 MAR 2014

Accepted 29 APR 2014

Accepted article online 5 MAY 2014

Published online 12 JUN 2014

Hemispheric comparison of cirrus cloud evolution using in situ measurements in HIAPER Pole-to-Pole Observations

Minghui Diao¹, Mark A. Zondlo^{2,3}, Andrew J. Heymsfield⁴, and Stuart P. Beaton⁵

¹Advanced Study Program/Earth Observing Laboratory, National Center for Atmospheric Research, Boulder, Colorado, USA, ²Department of Civil and Environmental Engineering, Princeton University, Princeton, New Jersey, USA, ³Center for Mid-Infrared Technologies for Health and the Environment, Princeton University, Princeton, New Jersey, USA, ⁴Mesoscale and Microscale Meteorology, National Center for Atmospheric Research, Boulder, Colorado, USA, ⁵Earth Observing Laboratory, National Center for Atmospheric Research, Boulder, Colorado, USA

Abstract Cirrus clouds' radiative forcing is highly sensitive to their microphysical properties and evolution. However, there are very limited data sets with both microscale resolution and global coverage to provide a hemispheric comparison of cirrus cloud microphysical properties and their evolution. Here we use in situ aircraft observations on the ~200 m scale from 87°N to 67°S over North America and the central Pacific Ocean to analyze the hemispheric differences in the evolution of cirrus clouds' horizontal segments—ice supersaturated regions (ISSRs) and ice crystal regions (ICRs). In contrast to previous in situ observations, we show that the clear-sky ice supersaturation frequency, resulting microphysical parameters (ice crystal size and concentration), and relative timescale of the life cycle of ISSRs and ICRs are similar between the Northern and Southern Hemispheres. More studies on hemispheric ice nuclei distributions and dynamical conditions are needed to help explain these observations.

1. Introduction

The radiative forcing of a cirrus cloud on the Earth's surface could be either cooling or warming, and its magnitude and direction are highly sensitive to the microphysical properties such as ice crystal number density (Nc), size distribution, and relative humidity with respect to ice (RH_i) [Liou, 1992; Fusina et al., 2007]. The evolution of these microphysical properties influences the overall radiative forcing throughout a cloud's lifetime, yet most of the climate models currently do not resolve these evolution processes at subgrid scale [e.g., Gettelman et al., 2010; Salzmann et al., 2010]. In fact, the limitation in the parameterization of cirrus cloud evolution on the microscale (~100 m) is partly due to the lack of analyses on the evolution of cirrus cloud microphysical properties. In particular, it is still an unsolved question of how the prerequisite conditions of cirrus cloud formation and the following cloud evolution processes would differ between the two hemispheres. Previous analyses using in situ observations at two locations (55°N Prestwick, Scotland, and 55°S Punta Arenas, Chile) compared the initial conditions of cirrus cloud formation, i.e., clear-sky ice supersaturation (ISS, where RH_i > 100%), as well as the microphysical properties of cirrus clouds in the two hemispheres [Ovarlez et al., 2002; Gayet et al., 2004]. Ovarlez et al. [2002] showed that the clear-sky ISS frequency is higher in the Southern Hemisphere (SH) than the Northern Hemisphere (NH), and Gayet et al. [2004] showed that the mean Nc of in-cloud conditions is higher in the NH than SH. However, these comparisons did not separate the ice supersaturated regions (ISSRs) and ice crystal regions (ICRs) between their earlier and later stages, such as large ISSRs with newly formed ice crystals versus fully developed ICRs with sparsely distributed ISS. Therefore, the previous analyses of the hemispheric differences in ISSRs and ICRs could be influenced by the sampling biases over different evolution phases of these regions. Other remote sensing analyses of Gettelman et al. [2006b] showed that the SH has higher clear-sky ISS frequency than the NH based on 3 year Atmospheric Infrared Sounder (AIRS) data, while Kahn et al. [2009] showed no clear difference between the two hemispheres using 1 year AIRS data. Kahn et al. [2009] pointed out that not only could the differences in sampling sizes lead to the different results but also the remote sensing retrievals could average out the hemispheric differences due to the coarse-scale resolution. Currently, there are no other high-resolution analyses to compare with the work of Ovarlez et al. [2002] and Gayet et al. [2004]. It is still not known whether the clear-sky ISS frequency differs between the two hemispheres at other regions and whether the evolution of cirrus cloud microphysical properties follows different paths between the two hemispheres.

To address the hemispheric differences in ice microphysical properties, all stages of their evolution need to be analyzed: the initial conditions of ice crystal formation—clear-sky ISS, the formation and growth of ice crystals inside ISS, and their sedimentation and sublimation. The analysis of microphysical processes requires observational data sets with microscale resolution, while the hemispheric comparison requires spatial coverage at the global scale. These requirements post a large challenge to current observational techniques. The remote sensing observations provide global-scale analyses of ISS [Gottelman *et al.*, 2006a; Kahn *et al.*, 2009; Lamquin *et al.*, 2012] as well as ice crystal properties [Kahn *et al.*, 2008; Liou *et al.*, 2008; Yue and Liou, 2009; Ou *et al.*, 2013], yet they usually suffer from coarse spatial resolution and uncertainties in water vapor measurements in the upper troposphere and lower stratosphere (UT/LS) [Susskind *et al.*, 2003; Gottelman *et al.*, 2004; Divakarla *et al.*, 2006; Diao *et al.*, 2013b]. On the other hand, in situ observations provide fast, high-resolution data sets but they usually suffer from the restrictions in sampling scales in space and time [Heymsfield *et al.*, 1998; Vömel *et al.*, 2002; Spichtinger *et al.*, 2003; Jensen *et al.*, 2005].

In this study, a global-scale aircraft-based data set [Wofsy *et al.*, 2011] is used to compare the microphysical properties of ISSRs and ICRs between the two hemispheres. Although the current data set is still limited in longitudinal coverage (92°W–128°E), it provides wide latitudinal coverage from 87°N to 67°S. In order to analyze the evolution of these microphysical processes, the method of Diao *et al.* [2013a] is used to help separate five phases of ISSR and ICR evolution, and each phase is compared individually between the NH and SH.

2. Data Set and Instrumentations

In this study we use the 1 Hz (~230 m) aircraft-based observations from the NSF Gulfstream-V (GV) research aircraft during the NSF High-Performance Instrumented Airborne Platform for Environmental Research (HIAPER) Pole-to-Pole Observations (HIPPO) Global campaign [Wofsy *et al.*, 2011]. The HIPPO Global campaign covers from 87°N to 67°S, sampling both the North America continent and the central Pacific Ocean. The HIPPO Global campaign provided ~400 h flight time and ~600 vertical transects from the surface to the tropical UT or the extratropical UT/LS. Four deployments of the HIPPO campaign were analyzed, including HIPPO#2 (October–November 2009), HIPPO#3 (March–April 2010), HIPPO#4 (June–July 2011), and HIPPO#5 (August–September 2011). HIPPO#1 was not included because no ice probe was part of the payload. The flights were over both land and ocean, yet most of the land area was over the continental North America, and the ocean area was mostly across the central Pacific Ocean between Alaska and New Zealand. All the samples were restricted to temperature $\leq -40^{\circ}\text{C}$ to exclude the coexistence of supercooled liquid water droplets with ice crystals. Most of the observations at temperature $\leq -40^{\circ}\text{C}$ are in the extratropical regions (~73.2 h) instead of the tropics (~18.0 h). In fact, because of the flight ceiling restriction (~15 km) of the GV research aircraft, only the base of the tropical tropopause layer was sampled in HIPPO.

Water vapor was measured by the 25 Hz, open-path Vertical Cavity Surface Emitting Laser (VCSEL) hygrometer [Zondlo *et al.*, 2010]. The water vapor measurements were averaged to 1 s for consistency with the temperature measurements. The accuracy and precision of water vapor measurements are ~6% and $\leq 1\%$, respectively. Temperature was recorded by a Rosemount total temperature probe (deiced model 102 LA) with the accuracy and precision of $\sim \pm 0.5$ K and 0.01 K, respectively. The RH_i uncertainties at 233.15–196 K were ~8–14% by combining the uncertainties in water vapor and temperature measurements. The probability distribution of our in-cloud RH_i observations peaks around 100% [Diao *et al.*, 2014], which is very consistent with previous 1 Hz aircraft observations [Ovarlez *et al.*, 2002; Krämer *et al.*, 2009]. The mean true air speed of the aircraft for current analyses was ~ 229 m s⁻¹. Ice crystals were measured by the 2DC ice probe, which reports ice crystal number density (N_c in #/L) and number-weighted mean diameter (D_c in micrometers) [Korolev *et al.*, 2011]. The physical range of the 64-diode 2DC is 25–1600 μm , and we applied a strict quality control, which filters out the particles below 100 μm in order to minimize the shattering effect. We tested our analyses for both with and without this strict quality control, and the conclusions on the hemispheric comparisons of ice microphysical properties do not vary. In addition, the lowest N_c detected in HIPPO is ~ 0.02 L⁻¹ (i.e., about half of a diode activated per second). To show that the hemispheric comparisons are not sensitive with this N_c threshold, a higher threshold of N_c > 0.1 L⁻¹ has also been tested and the conclusions do not vary. Ice supersaturated regions (ISSRs) are defined as where ISS is spatially continuously observed [Spichtinger *et al.*, 2005]. Ice crystal regions (ICRs) are defined as the locations where the ice particle concentrations are spatially continuously greater than 0.02 L⁻¹ during the 1 Hz measurements, while the remaining regions are considered to be clear-sky regions [Diao *et al.*, 2013a]. Here the ICRs represent horizontal segments of cirrus clouds, since the horizontal

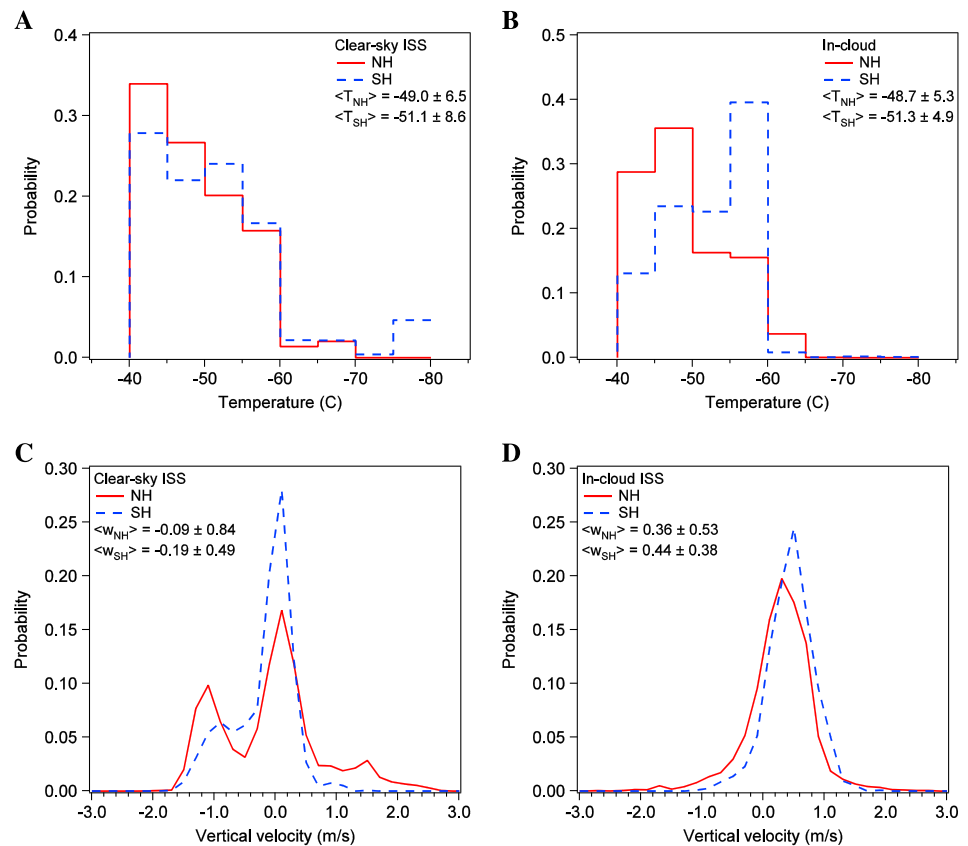


Figure 1. Histograms of (a, b) temperature (binned by 5°C) and (c, d) vertical velocity (binned by 0.2 m/s) at the clear-sky ISS condition (Figures 1a and 1c) and in-cloud condition (Figures 1b and 1d) for the NH (red solid line) and SH (blue dashed line). The means and standard deviations of temperature and vertical velocity are shown in the figure legend, where $\pm \sigma$ stands for ± 1 standard deviation.

true air speed of the aircraft is at least ~ 25 times larger than that in the vertical direction. The final data set includes ~ 65.1 h in the NH and ~ 26.1 h in the SH at $T \leq -40^\circ\text{C}$. Among these observations, there are ~ 5.5 h and ~ 1.3 h of ISS observations in the NH and SH and ~ 3.2 h and ~ 0.4 h of ICR observations in the NH and SH, respectively. The overlaps of ISS and ICR in the NH and SH are ~ 1.3 h and ~ 0.3 h, respectively.

Because the formation of ISS and ice crystals are influenced by temperature and vertical velocity distributions, we show the histograms of temperature and vertical velocity for both the clear-sky ISS and the in-cloud conditions (Figure 1). In general, the NH and SH have similar vertical velocity distributions for the clear-sky ISS and in-cloud conditions, while the SH has slightly lower mean temperatures at the clear-sky ISSRs and in-cloud conditions ($-51.1 \pm 8.6^\circ\text{C}$, $-51.3 \pm 4.9^\circ\text{C}$) than those in the NH ($-49.0 \pm 6.5^\circ\text{C}$, $-48.7 \pm 5.3^\circ\text{C}$), where the quoted uncertainty stands for 1 standard deviation. We note that this study has a different temperature range (-40 to -77°C) compared with that in Gayet *et al.* [2004] (-30 to -65°C), which has mean in-cloud temperatures at -46.0°C (NH) and -46.4°C (SH). The in-cloud vertical velocity distributions are similar between the two studies.

3. Method to Separate Five Phases of ISSR and ICR Evolution

In this study, we use the method from Diao *et al.* [2013a] to separate five evolution phases of ice crystal formation from the Eulerian observations, that is, clear-sky ISS, nucleation, early growth, later growth, and sedimentation/sublimation. In general, these five phases illustrate how clear-sky ISSRs (phase 1) evolve into small ICRs embedded in large ISSRs (phase 2), and as the ICRs expand in space, the ICRs and ISSRs become spatially intersected (phase 3); then the ICRs take over the space and small ISSRs are embedded in large ICRs (phase 4); finally, all water vapor in excess of ice saturation is depleted and ISSRs disappear, while ICRs sublimate in subsaturated regions (phase 5). The number of cases from phases 1 to 5 analyzed (particles $> 100 \mu\text{m}$) in the NH are 329, 51, 45, 32, and 1167 and in the SH are 209, 16, 20, 2, and 137, respectively. In total, there are 1624 and 384 cases of ISSR+ICR samples in the NH and SH, respectively.

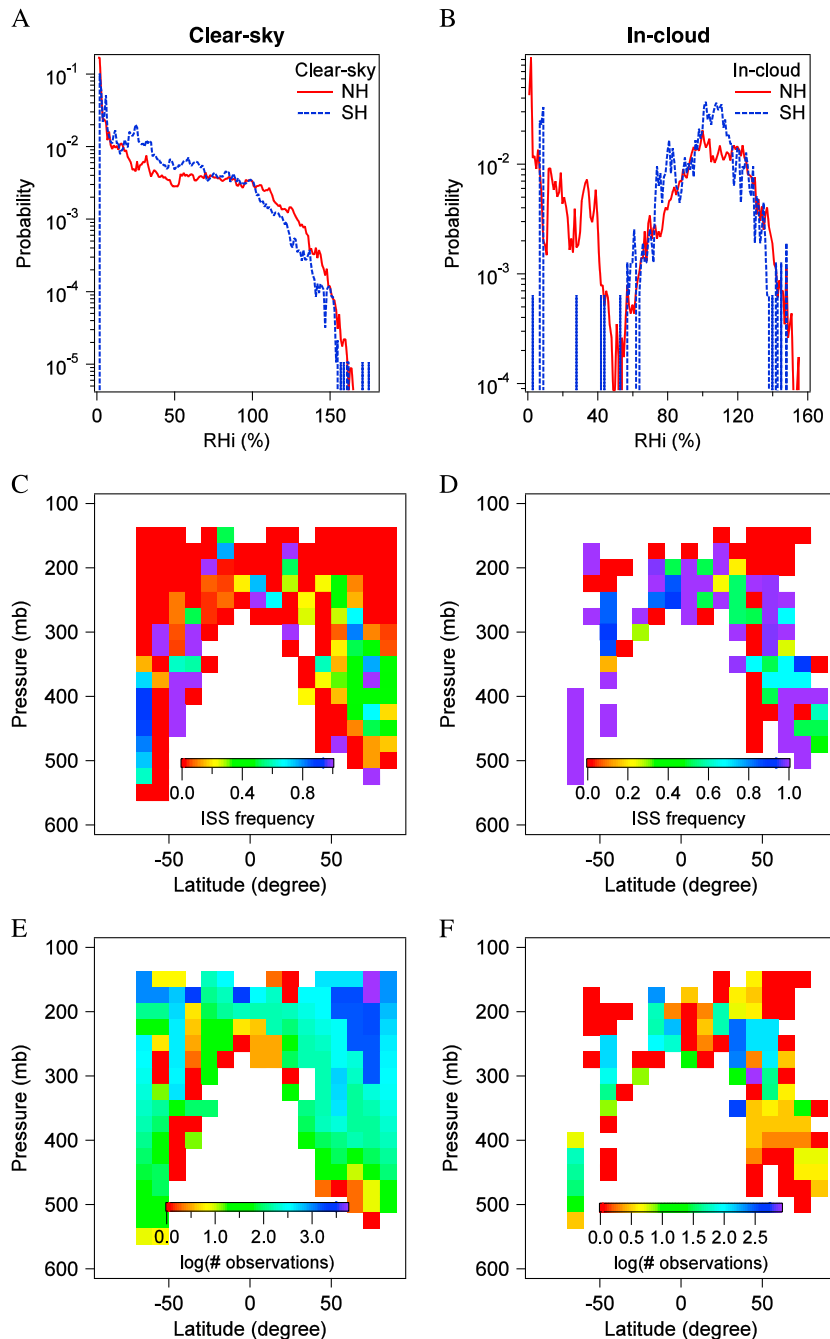


Figure 2. Comparisons of ISS distribution in the two hemispheres for HIPPO#2-5 separated into (a, c, e) clear-sky and (b, d, f) in-cloud conditions. (a, b) The histograms of RHI are plotted for the NH (red lines) and SH (blue) binned by 1%. (c, d) Latitudinal and vertical distributions of the ISS frequency are binned by 25 mb × 10°. ISS frequency in each bin is color coded from 0 (red) to 1 (purple). (e, f) The number of 1 Hz observations at T ≤ −40 °C on the log scale.

4. Results

4.1. Hemispheric Comparisons of Clear-Sky ISS Frequency Distribution

As the prerequisite conditions for ice nucleation, ISS can be used as an indicator for the hemispheric comparison of ice nucleation. To directly compare with the previous 1 Hz aircraft observations of *Ovarlez et al.* [2002], we compare the probability distributions of RHI between the two hemispheres for both clear-sky and in-cloud conditions (Figures 2a and 2b). We observed similar clear-sky ISS frequencies in the NH and SH, which is different from the observations of *Ovarlez et al.* [2002] that the clear-sky ISS frequency is higher in the SH than NH. For in-cloud

conditions, both our observations and *Ovarlez et al.* [2002] show similar peak values around 100% for the histograms of RHi in the two hemispheres. Since the HIPPO flight tracks are different from those in *Ovarlez et al.* [2002] (Punta Arenas, Chile, and Prestwick, Scotland), the differences between these two observations could result from different geographical locations, which points out the sensitivity of this type of analyses on the sampling domain. Yet because of the limitation in longitudinal coverage in this work, the zonal mean RHi distribution of the two hemispheres needs further investigation.

To further compare the latitudinal and vertical distribution of ISS frequency in the NH and SH, the clear-sky and in-cloud observations are separately binned into $25 \text{ mb} \times 10^\circ$ grids. The frequencies of ISS observations are color coded from 0 (red) to 1 (purple) in each bin for the clear-sky (Figure 2c) and in-cloud (Figure 2d) conditions. Consistent with the probability distribution analyses, there are similar ISS frequencies in the NH and SH for both clear-sky and in-cloud conditions. The number of observations of total clear-sky and in-cloud data is shown in log scale in Figures 2e and 2f, respectively, where the total clear-sky data ($T \leq -40^\circ\text{C}$) are $\sim 62.0 \text{ h}$ and $\sim 25.6 \text{ h}$ in the NH and SH and in-cloud data are $\sim 3.2 \text{ h}$ and $\sim 0.4 \text{ h}$ in the NH and SH, respectively. The number of bins with higher ISS frequency in the NH (or SH) is 27 (27) for clear-sky conditions and 8 (12) for in-cloud conditions. The statistical significance tests show that the probability of $P(X \geq 27)$ for a binomial distribution of $B(27 + 27, \frac{1}{2})$ is 0.55 and $P(X \geq 12)$ for $B(8 + 12, \frac{1}{2})$ is 0.25, which indicate no strong evidence against the null hypotheses. Thus, the ISS frequency is not significantly different between the NH and SH for both clear-sky and in-cloud conditions in the HIPPO campaign. Because of the large spatial variability of ISS frequency as previously observed in global AIRS retrievals [*Lamquin et al.*, 2012], we caution that our observations only represent the locations over the HIPPO sampling domain. Future flight campaigns over other regions such as Atlantic Ocean will help to improve our understanding of ISS distribution longitudinally.

4.2. Comparisons of RHi Evolution in Five Phases

To compare the ice microphysical properties and their evolution between the two hemispheres, we separate the aircraft observation in the Eulerian view into five evolution phases. Figure 3 shows the evolution of RHi in the NH (Figures 3a–3c) and SH (Figures 3d–3f) for the clear-sky ISS (phase 1; Figures 3a, 3d, and 3g), the ice crystal nucleation and growth (phases 2–4; Figures 3b, 3e, and 3h), and the sedimentation/sublimation (phase 5; Figures 3c, 3f, and 3i). Here we use the increasing length of clear-sky ISSRs to illustrate the expansion of ISSRs during the formation of clear-sky ISSRs (from left to right). Also, the increasing spatial ratio of ICR/ISSR is used to illustrate the expansion of ICRs with respect to ISSRs from the nucleation to growth phases (from left to right). The decreasing horizontal length of ICRs illustrates the shrinking sizes of ICRs in the sedimentation/sublimation phase (from right to left). The mean and standard deviation (1σ) RHi values in each size bin are shown as the black line and the black scale bars, respectively. Both hemispheres follow similar trends of RHi evolution, i.e., (1) increasing values of RHi with increasing horizontal length scale of clear-sky ISSRs, (2) decreasing RHi as ice crystals form and grow, and (3) widening of RHi distribution into drier conditions with the shrinking of ICRs during sedimentation/sublimation. In order to more quantitatively compare the RHi evolution between the NH and SH, the mean RHi values (red) and their differences (NH-SH) (blue) as a function of evolution are shown in Figures 3g–3i. To test the statistical significance of these differences in mean RHi values, we compared them against their 95% confidence intervals (blue scale bars in Figures 3g–3i). The 95% confidence interval is calculated as the product of the standard error (σ_{error}) of the hemispheric difference and the Student's T value ($T_{0.95, \text{df}-1}$) referring to a two-tailed normal distribution with a certain degree of freedom (df). Here σ_{error} is calculated based on two samples having possibly unequal variances, and df is calculated based on the Welch-Satterthwaite equation:

$$\sigma_{\text{error}} = \sqrt{\frac{\sigma_{\text{var1}}}{N_1} + \frac{\sigma_{\text{var2}}}{N_2}}; \quad \text{df} = \frac{\left(\frac{\sigma_{\text{var1}}}{N_1} + \frac{\sigma_{\text{var2}}}{N_2}\right)^2}{\frac{\sigma_{\text{var1}}^2}{N_1^2(N_1 - 1)} + \frac{\sigma_{\text{var2}}^2}{N_2^2(N_2 - 1)}}$$

Here σ_{var1} , σ_{var2} , N_1 , and N_2 are sample variances and sample sizes for the NH and SH, respectively. Based on the df values in the current sampling, most Student's T values are around 2. The results show that regardless of the slightly lower mean temperatures in the SH for the clear-sky ISS and in-cloud conditions, there are no statistically significant differences in the mean RHi values between the NH and SH as they are always smaller than the 95% confidence intervals. These results suggest that in addition to the initial conditions

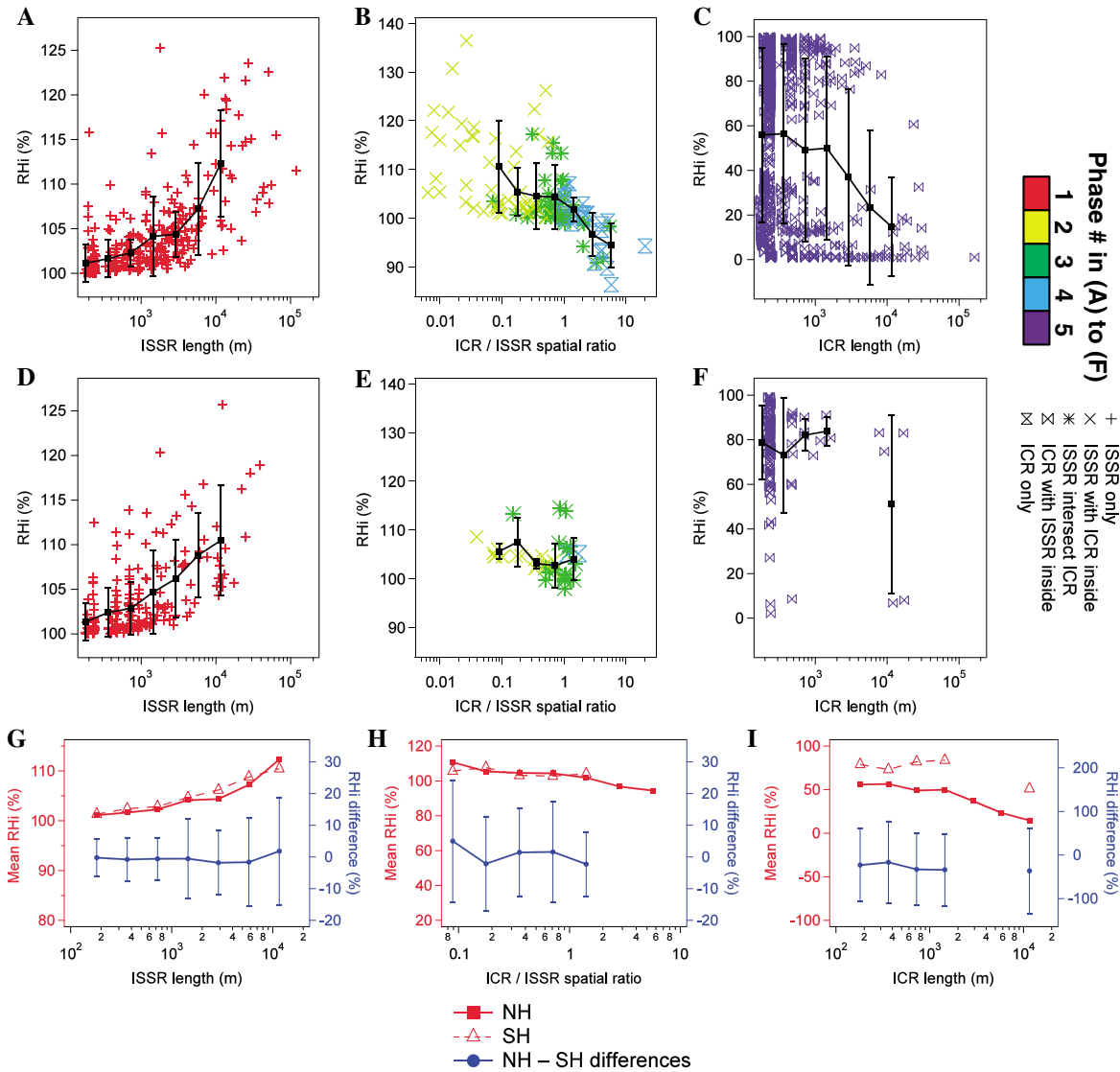


Figure 3. Comparisons of the RHi evolution phases between the (a–c) NH and (d–f) SH. Figures 3a and 3d are the clear-sky ISSR conditions (red markers); Figures 3b and 3e are the nucleation phase (yellow markers), early growth phase (green markers), and later growth phase (blue markers). Figures 3c and 3f are the sedimentation/sublimation phase (purple markers). All binning of length scales and spatial ratios used 2^i to 2^{i+1} bins ($i = \dots -1, 0, 1, 2, 3, \dots$), centered at $2^{i+0.5}$. The length-scale bins range from 2^7 (~100 m) to 2^{13} (~8200 m), and the ICR/ISSR spatial ratio ranges from 2^{-4} (0.0625) to 2^2 (4). The points outside these bin ranges are combined into the closest bins in order to reduce the sparsely distributed data. The black solid lines and the black scale bars in Figures 3a–3f show the means and standard deviations of RHi in each bin, respectively. The differences (NH–SH) of the means (blue line) and the 95% confidence intervals (blue scale bars) are shown on the right ordinate for (g) phase 1, (h) phases 2–4, and (i) phase 5. In Figures 3g–3i, the mean RHi values (red) are shown for the NH (solid line) and SH (dashed line) on the left ordinate.

of ice crystal formation (clear-sky ISS), the evolution of mean RHi value from ice crystal formation, growth to sedimentation is also comparable between the two hemispheres over the HIPPO sampling domain.

4.3. Comparisons of the Evolution of Ice Crystal Number Density and Mean Diameter

Besides the evolution of RHi, the evolution of ice crystal properties is analyzed in terms of N_c (in #/L) and D_c (in micrometers). As shown in Figure 4, the evolution of N_c (Figures 4a, 4b, 4e, 4f, 4i, and 4j) and D_c (Figures 4c, 4d, 4g, 4h, 4k, and 4l) are compared between the NH (Figures 4a–4d) and SH (Figures 4e–4f) for the nucleation/early growth/late growth phases (Figures 4a, 4c, 4e, 4g, 4i, and 4k) and the sedimentation/sublimation phase (Figures 4b, 4d, 4f, 4h, 4j, and 4l). We note that these N_c and D_c analyses filtered out particles smaller than 100 μm .

For both hemispheres, as ICRs gradually take over the space of ISSRs, the mean N_c values increase, which agrees with previous simulations that new ice crystals may continue to form with continuous uplifting [Spichtinger and

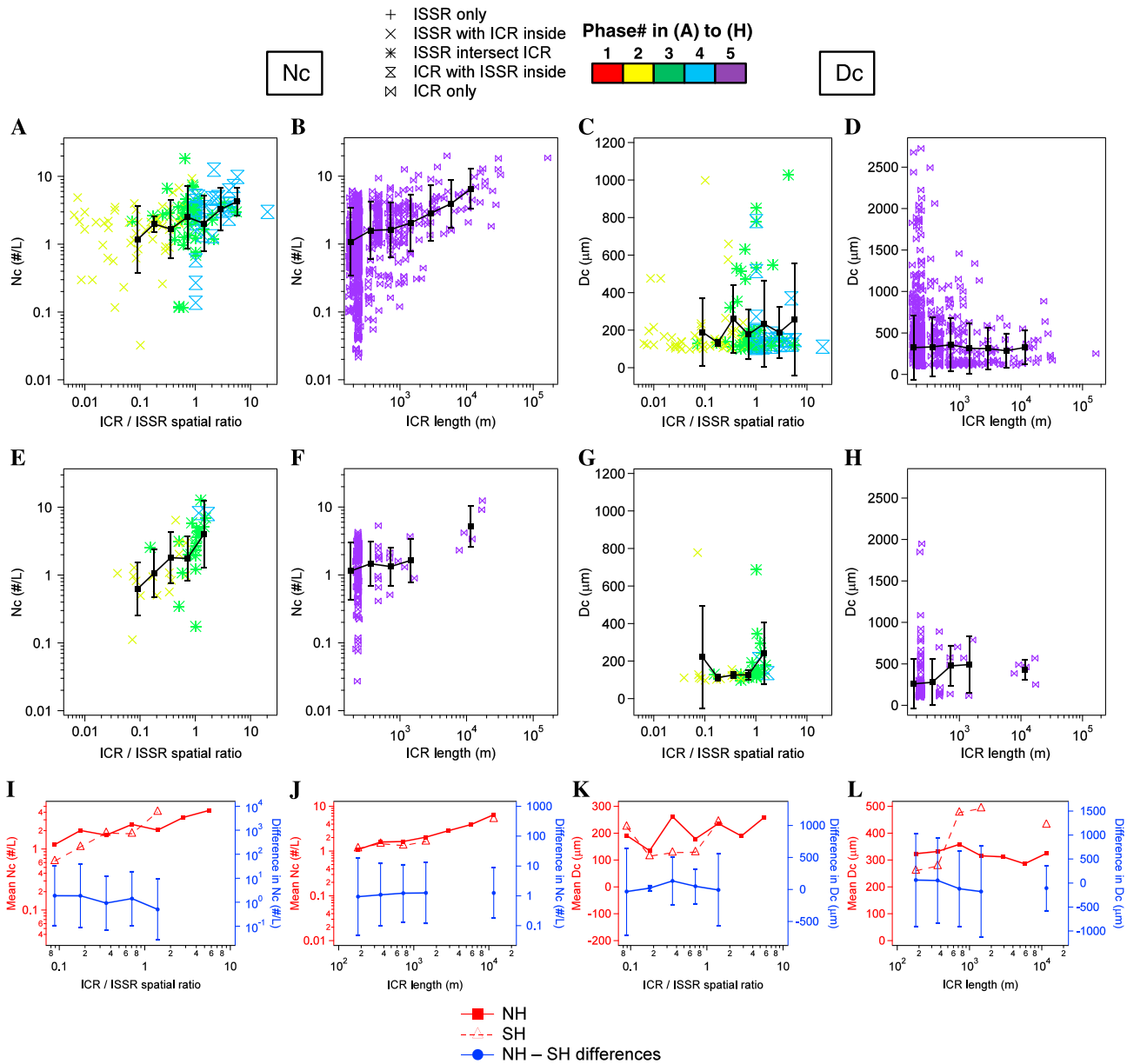


Figure 4. Evolution of ice crystal number density (Nc) and mean diameter (Dc) in the (a–d) NH and (e–h) SH. The bin ranges for the length scales and the ICR/ISSR spatial ratios are the same as those used in Figure 3, and the points outside these ranges are combined into the closest bins. The evolutions of Nc and Dc in phases 2 to 4 are shown in first and third columns, respectively. The evolutions of Nc and Dc in phase 5 are shown in second and fourth columns, respectively. (i–l) Similar to Figure 3, the mean Nc and Dc values for the NH (red solid line) and SH (red dashed line) are shown on the left ordinate. The differences (NH–SH) of the means (blue line) and the 95% confidence intervals (blue scale bars) are shown on the right ordinate. The color coding and marker in Figure 4 are similar to Figure 3.

Gierens, 2009]. In addition, during sedimentation/sublimation, both hemispheres show a widening range of Nc distribution, indicating that not all aged ICRs experienced the same dissipation processes. For the evolution of Dc, both hemispheres show that the mean values of Dc in the nucleation and growth phases are almost constant, which agrees with the theoretical growth of ice crystals via water vapor diffusion [Rogers and Yau, 1989; Straka, 2009], that is, the growth rate of a single ice crystal is inversely related to its size, which means that smaller ice crystals will have faster growth rates and eventually catch up in size with the larger ice crystals. In addition, during sedimentation/sublimation, the range of Dc widens, which suggests a separation between smaller and larger ice crystals into different vertical levels.

To show the comparison of Nc and Dc evolution more clearly between the NH and SH, their means, differences in means, and the 95% confidence intervals for these differences are shown in Figures 4i–4l. Similar to the

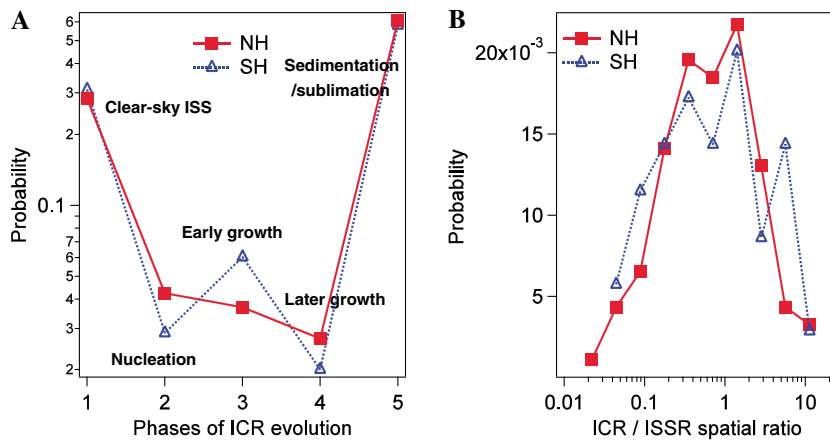


Figure 5. Probability of the ISSR and ICR evolution phases in the NH (red solid line) and SH (blue dotted line). (a) Probability of phases 1 to 5, normalized by the total ISSR + ICR samples (including the whole size range of 2DC) of 920 and 348 in the NH and SH, respectively. (b) Probability for each bin of the ICR/ISSR spatial ratio, also normalized by the total ISSR + ICR number in each hemisphere.

RHi evolution comparison, the hemispheric differences in the mean values of N_c and D_c are always within the 95% confidence intervals. These results are different from Gayet *et al.* [2004], which observed higher N_c and lower effective diameter in the NH for the mean state of ICRs. We note that the sampling differences could contribute to the differences in N_c and D_c comparisons between these two studies, including differences in temperature range, geographical location, and different ice crystal size ranges (100–1600 μm in this work versus 3–21.8 μm plus 25–800 μm in Gayet *et al.* [2004]). More investigation is needed to determine the influences of each of these sampling differences.

4.4. Comparisons of Relative Timescale and Spatial Expansion of Five Phases

The ratio of the sample size of each evolution phase with respect to the total number of samples over all evolution phases indicates the relative timescale of each ISSR + ICR evolution phase. Because the definition of ICRs is based on the presence of ice crystals instead of their sizes, we include ice crystals within the whole 2DC measurement range for the ISSR + ICR evolution timescale analyses. Figure 5a shows the probability of phases 1 to 5, normalized by the total number of ISSR + ICR samples of 920 and 348 in the NH (red solid line) and SH (blue dotted line), respectively. The clear-sky ISSRs (phase 1), the coexisting ISSRs and ICRs (phases 2, 3, and 4), and the subsaturated ICRs (phase 5) each contribute to 28%, 11%, and 61% of the total ISSR + ICR samples in the NH, which is comparable to those of 31%, 11%, and 58% in the SH. Both hemispheres show timescale ratios of ISSR + ICR evolution comparable to those in previous simulations of 30%, 10%, and 60% [Spichtinger and Gierens, 2009]. In addition, the probability of each length ratio of ICR/ISSR normalized by the total number of ISSR + ICR samples is shown in Figure 5b, which illustrates the relative timescale of ICR length expansion. The probabilities of ICR/ISSR spatial ratio in the NH and SH both peak around 1. These analyses suggest that the observations in HIPPO not only show similar relative timescales for each ISSR + ICR evolution phase between the two hemispheres but also show similar relative timescales for ICRs to expand to a certain length ratio with respect to ISSRs. The similarities in the relative timescales of ISSR and ICR evolution between the NH and SH may be a result of similar dynamical conditions, such as the similar vertical velocity distributions for the clear-sky ISS and in-cloud conditions. Yet more case studies are needed to assess the influences from specific dynamics such as turbulence and large-scale waves.

5. Implications for Studies on Ice Microphysics Between the Two Hemispheres

Based on the observations of HIPPO campaign over North America and the central Pacific Ocean, we found that the initial conditions of ice crystal formation, clear-sky ISS, have similar frequency distributions between the NH and SH. In addition, the evolution of the ice microphysical properties is similar, as we compared the mean values of RHi, N_c , and D_c as a function of the ISSR and ICR evolution. We caution that there are limitations in the current method of converting the 1-D Eulerian observations into the evolutionary view. For example, the ICRs here only represent horizontal segments of cirrus clouds, while the evolution of vertical

segments has not been addressed. Further, the relative timescales of ICRs during each evolution phases do not equally represent the lifetime of cirrus clouds, since the early and later stages of ICRs can coexist in one cloud. In addition, the current analysis suggests that the hemispheric comparisons are sensitive to the sampling domain, which points out the importance of additional in situ observations across large longitudinal and latitudinal domains. The resolution of the observations may also influence the analyses of ISS and ice microphysics as *Kahn et al.* [2009] pointed out. Thus, more analyses are needed in the future to address the influence of coarse resolution to the observed evolution of ISSRs and ICRs.

Besides the sampling domain and resolution, other factors such as large-scale dynamics, seasonal variability, land versus ocean differences, and aerosol indirect effects also influence the comparisons of ice microphysical properties between the two hemispheres, which require more study to separately address these influences. For example, *Cziczo et al.* [2013] reported the efficiency of different aerosols acting as ice nuclei (IN) for ice crystal formation, which suggests that the hemispheric differences in aerosol content and concentration could lead to different ice microphysics. Future analyses are needed to address whether the hemispheric differences in ice nuclei loading would directly influence the formation and evolution of ice crystals or whether the SH has sufficient amount of efficient IN even though the aerosol optical depth in the SH is ~ 1 order of magnitude smaller than that in the NH [*Clarke and Kapustin*, 2010]. Ultimately, more modeling work is needed at spatial and temporal scales comparable to observations to conduct direct comparisons between the simulated and observed ISSR and ICR evolution.

Acknowledgments

We gratefully acknowledge funding for field support and data analyses from the following sources: NSF AGS-1036275 for VCSEL hygrometer in the HIPPO Global campaign. M.D. gratefully acknowledges support from the NASA Earth and Space Science Graduate Fellowship (NNX09AO51H), Walbridge Fund Graduate Award, and the National Center for Atmospheric Research (NCAR) Advanced Study Program (ASP) postdoctoral fellowship. The National Center for Atmospheric Research is sponsored by the National Science Foundation (NSF). We appreciate the efforts of NCAR EOL flight, technical, and mechanical crews during HIPPO Global campaign, in particular the PIs of the HIPPO Global campaign: S. Wofsy, R. Keeling, and B. Stephens. We acknowledge the support of 2DC probe by C. J. Webster and D. C. Rogers, and P. Romashkin for field support of the VCSEL hygrometer. We also appreciate helpful discussions with L. Donner, J. B. Jensen, L. L. Pan, R. B. Friesen, and W. A. Cooper. Final data sets and documentation from the NSF HIPPO campaign can be accessed at <<http://hippo.ornl.gov>> in the Carbon Dioxide Information Analysis Center Data Archive at Oak Ridge National Laboratory.

The Editor thanks two anonymous reviewers for their assistance in evaluating this paper.

References

- Clarke, A., and V. Kapustin (2010), Hemispheric aerosol vertical profiles: Anthropogenic impacts on optical depth and cloud nuclei, *Science*, **329**(5998), 1488–1492, doi:10.1126/science.1188838.
- Cziczo, D. J., K. D. Froyd, C. Hoose, E. J. Jensen, M. Diao, M. A. Zondlo, J. B. Smith, C. H. Twohy, and D. M. Murphy (2013), Clarifying the dominant sources and mechanisms of cirrus cloud formation, *Science*, **340**(6138), 1320–1324, doi:10.1126/science.1234145.
- Diao, M., M. A. Zondlo, A. J. Heymsfield, S. P. Beaton, and D. C. Rogers (2013a), Evolution of ice crystal regions on the microscale based on in situ observations, *Geophys. Res. Lett.*, **40**, 3473–3478, doi:10.1002/grl.50665.
- Diao, M., L. Jumbam, J. Sheffield, E. F. Wood, and M. A. Zondlo (2013b), Validation of AIRS/AMSU-A water vapor and temperature data with in situ aircraft observations from the surface to UT/LS from 87°N–67°S, *J. Geophys. Res. Atmos.*, **118**, 6816–6836, doi:10.1002/jgrd.50483.
- Diao, M., M. A. Zondlo, A. J. Heymsfield, L. M. Avallone, M. E. Paige, S. P. Beaton, T. Campos, and D. C. Rogers (2014), Cloud-scale ice supersaturated regions spatially correlate with high water vapor heterogeneities, *Atmos. Chem. Phys.*, **14**, 1–18, doi:10.5194/acp-14-1-2014.
- Divakarla, M. G., C. D. Barnett, M. D. Goldberg, L. M. McMillin, E. Maddy, V. Wolf, L. Zhou, and X. Liu (2006), Validation of Atmospheric Infrared Sounder temperature and water vapor retrievals with matched radiosonde measurements and forecasts, *J. Geophys. Res.*, **111**, D09S15, doi:10.1029/2005JD006116.
- Fusina, F., P. Spichtinger, and U. Lohmann (2007), Impact of ice supersaturated regions and thin cirrus on radiation in the midlatitudes, *J. Geophys. Res.*, **112**, D24S14, doi:10.1029/2007JD008449.
- Gayet, J. F., J. Ovarlez, V. Shcherbakov, J. Strom, U. Schumann, A. Minikin, F. Aurioi, A. Petzold, and M. Monier (2004), Cirrus cloud microphysical and optical properties at southern and northern midlatitudes during the INCA experiment, *J. Geophys. Res.*, **109**, D20206, doi:10.1029/2004JD004803.
- Gottelman, A., et al. (2004), Validation of Aqua satellite data in the upper troposphere and lower stratosphere with in situ aircraft instruments, *Geophys. Res. Lett.*, **31**, L22107, doi:10.1029/2004GL020730.
- Gottelman, A., W. D. Collins, E. J. Fetzer, A. Eldering, F. W. Irion, P. B. Duffy, and G. Bala (2006a), Climatology of upper-tropospheric relative humidity from the Atmospheric Infrared Sounder and implications for climate, *J. Clim.*, **19**(23), 6104–6121, doi:10.1175/JCLI3956.1.
- Gottelman, A., E. J. Fetzer, A. Eldering, and F. W. Irion (2006b), The global distribution of supersaturation in the upper troposphere from the Atmospheric Infrared Sounder, *J. Clim.*, **19**(23), 6089–6103, doi:10.1175/JCLI3955.1.
- Gottelman, A., X. Liu, S. J. Ghan, H. Morrison, S. Park, A. J. Conley, S. A. Klein, J. Boyle, D. L. Mitchell, and J.-L. F. Li (2010), Global simulations of ice nucleation and ice supersaturation with an improved cloud scheme in the Community Atmosphere Model, *J. Geophys. Res.*, **115**, D18216, doi:10.1029/2009JD013797.
- Heymsfield, A. J., L. M. Miloshevich, C. Twohy, G. Sachse, and S. Oltmans (1998), Upper-tropospheric relative humidity observations and implications for cirrus ice nucleation, *Geophys. Res. Lett.*, **25**(9), 1343–1346, doi:10.1029/98GL01089.
- Jensen, E., L. Pfister, T. Bui, A. Weinheimer, E. Weinstock, J. Smith, J. Pittman, D. Baumgardner, P. Lawson, and M. J. McGill (2005), Formation of a tropopause cirrus layer observed over Florida during CRYSTAL-FACE, *J. Geophys. Res.*, **110**, D03208, doi:10.1029/2004JD004671.
- Kahn, B. H., C. K. Liang, A. Eldering, A. Gottelman, Q. Yue, and K. N. Liou (2008), Tropical thin cirrus and relative humidity observed by the Atmospheric Infrared Sounder, *Atmos. Chem. Phys.*, **8**(6), 1501–1518, doi:10.5194/acp-8-1501-2008.
- Kahn, B. H., A. Gottelman, E. J. Fetzer, A. Eldering, and C. K. Liang (2009), Cloudy and clear-sky relative humidity in the upper troposphere observed by the A-train, *J. Geophys. Res.*, **114**, D00H02, doi:10.1029/2009JD011738.
- Korolev, A. V., E. F. Emery, J. W. Strapp, S. G. Cober, G. A. Isaac, M. Wasey, and D. Marcotte (2011), Small ice particles in tropospheric clouds: Fact or artifact? Airborne icing instrumentation evaluation experiment, *Bull. Am. Meteorol. Soc.*, **92**(8), 967–973, doi:10.1175/2010BAMS3141.1.
- Krämer, M., et al. (2009), Ice supersaturations and cirrus cloud crystal numbers, *Atmos. Chem. Phys.*, **9**(11), 3505–3522.
- Lamquin, N., C. J. Stubenrauch, K. Gierens, U. Burkhardt, and H. Smit (2012), A global climatology of upper-tropospheric ice supersaturation occurrence inferred from the Atmospheric Infrared Sounder calibrated by MOZAIC, *Atmos. Chem. Phys.*, **12**(1), 381–405, doi:10.5194/acp-12-381-2012.
- Liou, K. N. (1992), *Radiation and Cloud Processes in the Atmosphere*, pp. 255–339, Oxford Univ. Press, New York.
- Liou, K. N., Y. Gu, Q. Yue, and G. McFarguhar (2008), On the correlation between ice water content and ice crystal size and its application to radiative transfer and general circulation models, *Geophys. Res. Lett.*, **35**, L13805, doi:10.1029/2008GL033918.

- Ou, S. S. C., B. H. Kahn, K.-N. Liou, Y. Takano, M. M. Schreier, and Q. Yue (2013), Retrieval of cirrus cloud properties from the Atmospheric Infrared Sounder: The k-coefficient approach using cloud-cleared radiances as input, *IEEE Trans. Geosci. Remote Sens.*, *51*(2), 1010–1024, doi:10.1109/TGRS.2012.2205261.
- Ovarlez, J., J. F. Gayet, K. Gierens, J. Strom, H. Ovarlez, F. Auriol, R. Busen, and U. Schumann (2002), Water vapour measurements inside cirrus clouds in Northern and Southern Hemispheres during INCA, *Geophys. Res. Lett.*, *29*(16), 1813, doi:10.1029/2001GL014440.
- Rogers, R. R., and M. K. Yau (1989), *A Short Course in Cloud Physics*, 3rd ed., pp. 150–169, Pergamon Press, Oxford, U. K.
- Salzmann, M., Y. Ming, J.-C. Golaz, P. A. Ginoux, H. Morrison, A. Gettelman, M. Krämer, and L. J. Donner (2010), Two-moment bulk stratiform cloud microphysics in the GFDL AM3 GCM: Description, evaluation, and sensitivity tests, *Atmos. Chem. Phys.*, *10*, 8037–8064, doi:10.5194/acp-10-8037-2010.
- Spichtinger, P., and K. M. Gierens (2009), Modelling of cirrus clouds—Part 2: Competition of different nucleation mechanisms, *Atmos. Chem. Phys.*, *9*, 2319–2334.
- Spichtinger, P., K. Gierens, U. Leiterer, and H. Dier (2003), Ice supersaturation in the tropopause region over Lindenberg, Germany, *Meteorol. Z.*, *12*(3), 143–156, doi:10.1127/0941-2948/2003/0012-0143.
- Spichtinger, P., K. Gierens, and A. Dörnbrack (2005), Formation of ice supersaturation by mesoscale gravity waves, *Atmos. Chem. Phys.*, *5*(5), 1243–1255, doi:10.5194/acp-5-1243-2005.
- Straka, J. M. (2009), *Cloud and Precipitation Microphysics—Principles and Parameterizations*, 1st ed., Cambridge Univ. Press, Cambridge, New York.
- Susskind, J., C. D. Barnet, and J. M. Blaisdell (2003), Retrieval of atmospheric and surface parameters from AIRS/AMSU/HSB data in the presence of clouds, *IEEE Trans. Geosci. Remote Sens.*, *41*(2), 390–409, doi:10.1109/TGRS.2002.808236.
- Vömel, H., et al. (2002), Balloon-borne observations of water vapor and ozone in the tropical upper troposphere and lower stratosphere, *J. Geophys. Res.*, *107*(D14), 4210, doi:10.1029/2001JD000707.
- Wofsy, S. C., et al. (2011), HIAPER Pole-to-Pole Observations (HIPPO): Fine-grained, global-scale measurements of climatically important atmospheric gases and aerosols, *Philos. Trans. R. Soc., A*, *369*(1943), 2073–2086, doi:10.1098/rsta.2010.0313.
- Yue, Q., and K. N. Liou (2009), Cirrus cloud optical and microphysical properties determined from AIRS infrared spectra, *Geophys. Res. Lett.*, *36*, L05810, doi:10.1029/2008GL036502.
- Zondlo, M. A., M. E. Paige, S. M. Massick, and J. A. Silver (2010), Vertical cavity laser hygrometer for the National Science Foundation Gulfstream-V aircraft, *J. Geophys. Res.*, *115*, D20309, doi:10.1029/2010JD014445.